Dual-filament initiation of a Coronal Mass Ejection: observations and model

A.M. Uralov, S.V. Lesovoi, V.G. Zandanov and V.V. Grechnev
Institute of Solar-Terrestrial Physics, P.O. Box 4026, Irkutsk 664033, Russia

Abstract.

We propose a new model for the initiation of solar coronal mass ejections (CMEs) and CME-associated flares. The model is inferred from observations of a quiescent filament eruption in the north-western quadrant of the solar disk on 4 September 2000. The event was observed with Siberian Solar Radio Telescope (5.7 GHz), Nobeyama Radioheliograph (17 GHz) and SOHO/EIT & LASCO. Based on the observations, we suggest that the eruption could be caused by the interaction of two dextral filaments. According to our model, these two filaments merge together to form a dual-filament system tending to form a single long filament. This results in a slow upward motion of the dual-filament system. Its upward expansion is prevented by the attachment of the filaments to the photosphere by filament barbs as well as by overlying coronal arcades. The initial upward motion is caused by the backbone magnetic field (*first driving factor*) which connects the two merging filaments. Its magnetic flux increases slowly due to magnetic reconnection of the cross-interacting legs of these filaments. If a total length of the dual-filament system is large enough, then the filament barbs detach themselves from the solar surface due to magnetic reconnection between the barbs with oppositely directed magnetic fields. The detachment of the filament barbs completes the formation of the eruptive filaments themselves and determines the helicity sign of their magnetic fields. The appearance of a helical magnetic structure creates an additional upward-directed force (*second driving factor*). A combined action of the these two factors causes acceleration of the dual-filament system. If the lifting force of the two factors is sufficient to extend substantially the overlying coronal magnetic arcade, then magnetic reconnection starts below the eruptive filament in accordance with the classical scheme, and the *third driving factor* comes into play.

1. Introduction

Prominence eruptions or *disparitions brusques* are qualified as large-scale eruptive phenomena which occur in the solar atmosphere. Prominence eruptions, in turn, are constituents of coronal mass ejections (CMEs). Large solar flares accompany the development of CMEs in many cases. These phenomena are all interrelated and, perhaps, are different manifestations of a single physical process. Theoretical understanding of the causes of CME formation relies largely on observational facts accumulated over the last two decades. Nevertheless, a model hardly exists at the present time which could explain *how* and *why* a filament erupts (see, e.g., reviews by Forbes, 2000; Hudson, 1999;

Kučera and Antiochos, 1999; Švestka, 1999). One reason for this is a difficulty of observing CME manifestations near the solar surface, especially when CMEs occur on the solar disk. In spite of the recent progress (e.g., Hanaoka et al., 1994; Maia et al., 1999; Pohjolainen et al., 2001; reviews by Gopalswamy, 1999 and Pick, 1999), new experimental material is still important.

We present the observations of a filament eruption on the solar disk on 4 September 2000, which caused a CME and CME-associated flare. We discuss also a phenomenological model for the CME initiation inferred from observational data. Experimental material is based mainly on data from Siberian Solar Radio Telescope, SSRT (5.7 GHz; Krissinel et al., 2000). Eruptive filaments on the solar disk were observed with SSRT previously (Maksimov and Nefedyev, 1992). However, the event described below is the most successful due to the conditions and quality of the observations. The sensitivity of the SSRT is 800 K. With a solar disk brightness temperature of $\simeq$ 16000 K, it is sufficient for reliable observations of quiescent filaments whose brightness temperatures are $(5-12)\times10^3$ K (Zandanov and Lesovoi, 1999). The angular resolution of the SSRT in the two-dimensional mode was $\simeq 22''$, and the temporal resolution was 1–3 minutes. Analysis of the SSRT data is supplemented by their comparisons with solar images produced by Nobeyama Radioheliograph (NoRH) at 17 GHz and SOHO/EIT & LASCO accessible through the Internet. TRACE did not observe this event.

2. Observations

The filament that served as a source for the CME was in the quiescent state starting from its appearance on the solar disk on 26 August 2000. On 4 September, the filament lay in the western area of a giant filament channel extending behind the north-east limb. The position of this filament is indicated by the arrow on the Hα filtergram produced at Big Bear Solar Observatory (Fig. 1, top). The Hα image was taken about 13 hours before the activation of the filament on 4 September at about 04:55 UT according to microwave observations as well as to SOHO/EIT 195 Å images of lower cadence (12 min., CME Watch program). Another Hα image produced at Kanzelhoehe Solar Observatory after the filament eruption (06:32 UT, Fig. 1, middle) shows flare ribbons on both sides of the photospheric inversion line. Fig. 1 (bottom) shows an image at 5.7 GHz produced at the same time.

Figs. 2 and 3 illustrate the microwave observations of the event at 17 GHz (NoRH) and 5.7 GHz. One should keep in mind that the range of observed brightness temperatures at 5.7 GHz is more than

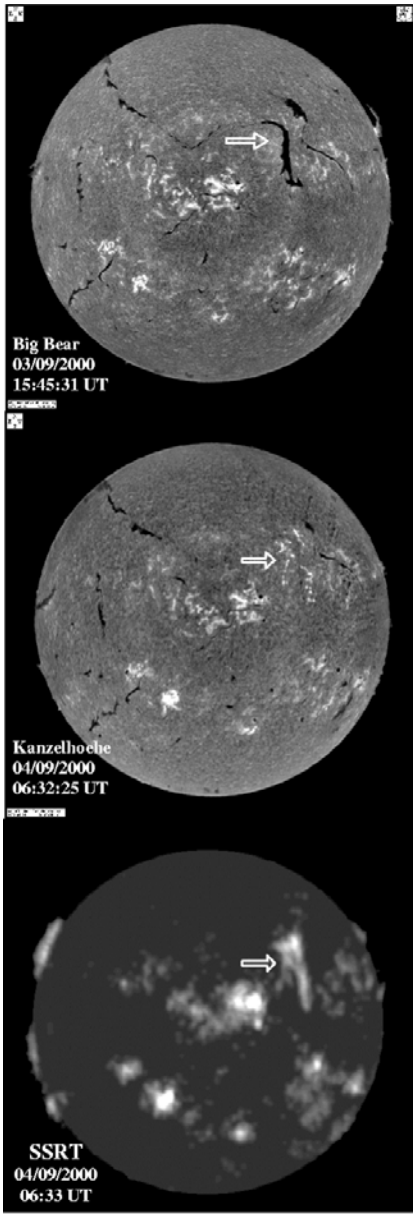

Figure 1. Top: Hα filtergram of the solar disk. Big Bear Solar Observatory, 15:46 UT, 3 Sept. The arrow indicates the position of the filament prior to eruption. *Middle*: Hα image one hour after the filament eruption. Kanzelhoehe Solar Observatory, 06:32 UT, 4 Sept. The arrow indicates the position of the flare ribbons well visible on both sides of the filament channel. *Bottom*: 5.7 GHz image of the solar disk. Siberian Solar Radio Telescope, 06:33 UT, 4 Sept. One can see a similarity between the microwave and Hα images of the two-ribbon flare (arrow).

one order of magnitude wider than that at 17 GHz, and to show better the low-contrast eruptive filament, we cut the brightness of solar radio sources in 5.7 GHz images from above. This results in the blurring of artificially saturated radio sources. The top left images correspond to the activation stage, when a motion of the dark filament (indicated by the arrow) is faintly visible. Subsequent images clearly show the movement of the eruptive filament and the development of the two-ribbon flare.

2.1. Shape and temperature of the eruptive filament

The images of the eruptive filament at 5.7 GHz and 17 GHz are similar. This is due to the opacity of the bulk of the filament at both of these frequencies (the first five images in Figs. 2 and 3). However, the eruptive filament at 5.7 GHz looks somewhat broader than at 17 GHz. This fact is known from radio observations of quiescent filaments (Gary; Zandanov, Lesovoi and Uralov, 1999). The difference can be associated in this case with manifestations of thin layers of cold material of $(6 - 8) \times 10^3$ K in the structure of the rapidly expanding filament. Remaining opaque at 5.7 GHz, these fragments of the filament become optically thin at 17 GHz. This is likely to be the main reason for the difference of the last images in Figs. 2 and 3 (at about 05:47 UT). The southern part of the filament is well visible on the solar disk at 5.7 GHz, but at 17 GHz it actually disappears. An essential broadening of the filament and increase of its transparency is also well visible in SOHO/EIT 195 Å images (two upper panels in Fig. 4). A helical structure that is being formed is detectable, and the solar disk is seen through this structure. At 05:48, the transparency of the filament becomes so high at 195 Å that the filament is almost invisible on the solar disk.

Typical brightness temperatures of dark fragments of the eruptive filament at 5.7 GHz on the solar disk are $\simeq (6 - 8) \times 10^3$ K, whereas outside of the solar limb they do not exceed $(4 - 5) \times 10^3$ K. Their brightness temperatures at 17 GHz are widespread, being lower than those at 5.7 GHz. This reflects the fact that the brightness temperatures of quiescent filaments at 17 GHz are lower by $(1 - 1.5) \times 10^3$ K than those at 5.7 GHz (Zandanov, Lesovoi and Uralov, 1999). Because of inhomogeneity and variability of the brightness temperature of the eruptive filament at 5.7 GHz, we cannot conclude whether the eruptive filament undergoes cooling or not. We can only state that the bulk of the eruptive filament is, at least, not heated. Moreover, there is certainly a hint of the following poorly pronounced effect. A minimum of brightness temperatures for some portions of the filament is reached just after the takeoff of the filament from the solar surface, when its

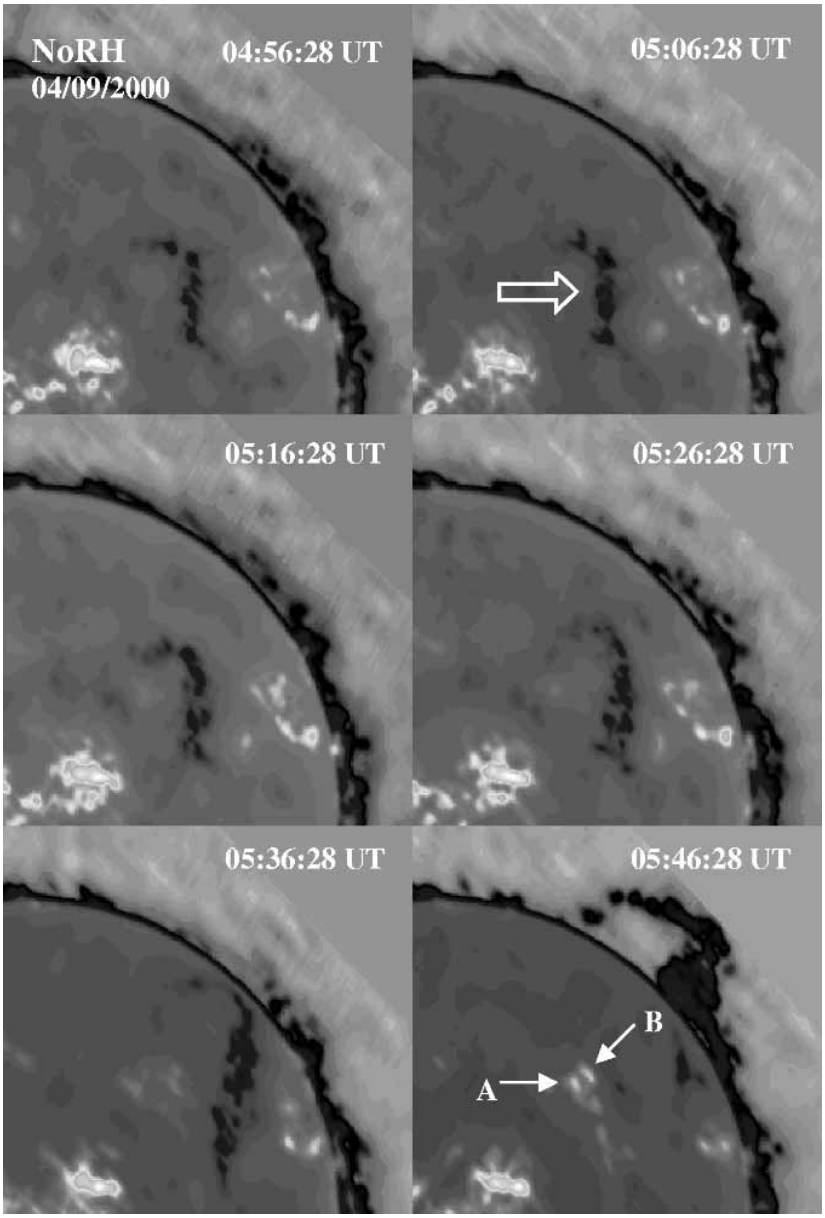

Figure 2. Sequence of 17 GHz images obtained with Nobeyama Radioheliograph. The top left image corresponds to the stage when the movement of the dark filament is faintly visible. The time interval between images is 10 min. The eruptive filament is indicated by the arrow. The two-ribbon flare started in microwave sources labeled **A** and **B**. The images are non-linearly processed to emphasize the features under discussion.

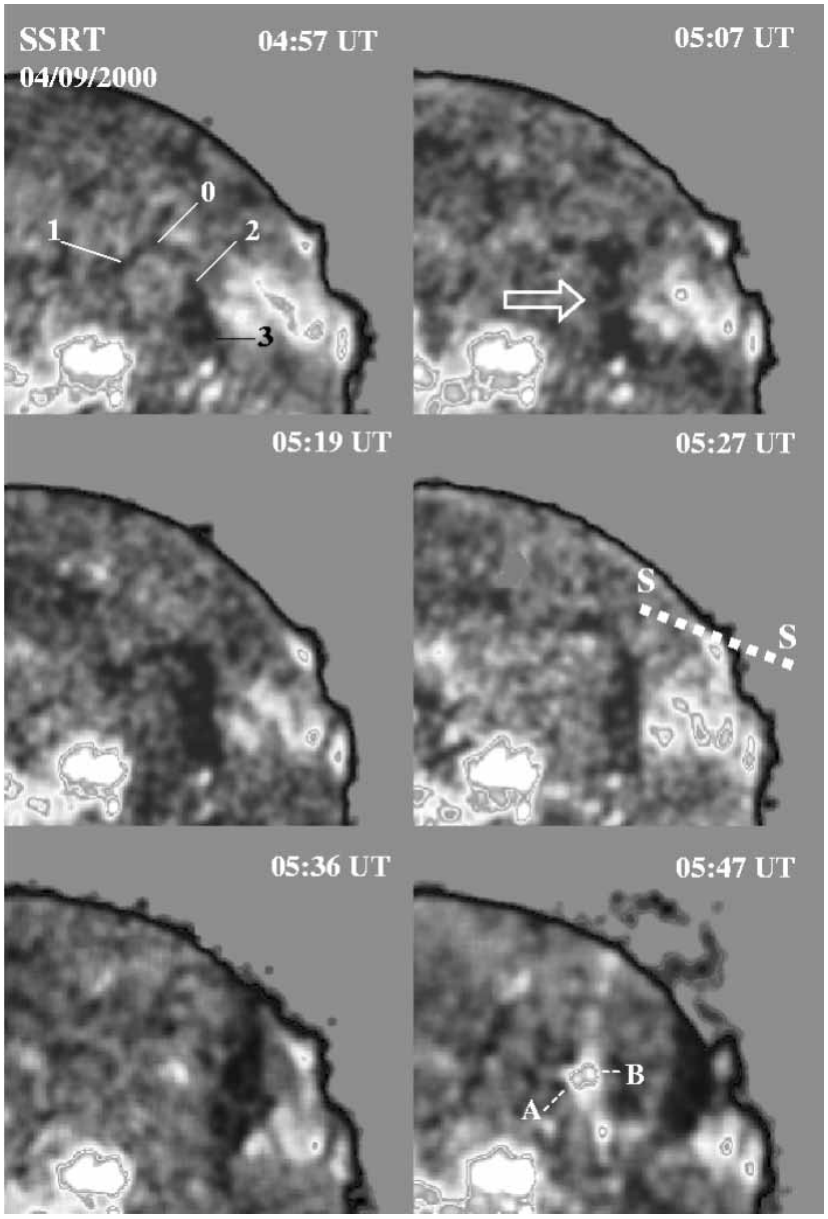

Figure 3. Sequence of 5.7 GHz images obtained with Siberian Solar Radio Telescope. The times indicated correspond to the passages of the eruptive filament across the SSRT beam. The eruptive filament (indicated by the arrow) initially appears as a single large expanding loop (first five images). Actually, it is an envelope of two filaments which developed subsequently (05:47 UT; see also Fig. 7). Labels 0–3 correspond to the initial positions of the filament's fragments, for which curves $R0-R3$ in Fig. 8 were constructed. The images are non-linearly processed to emphasize the features under discussion.

velocity increases (see Sections 2.4 and 2.5). The brightness temperature at that time is slightly lower than in the quiescent state. A slight darkening of the filament by a few hundred Kelvin at the onset of the movement was also found at 17 GHz by Gopalswamy, Hanaoka and Lemen (1998) who measured the mean brightness temperature over an area including both the eruptive filament and the quiet Sun. At the both frequencies, the decrease of the brightness temperature can be merely due to expansion of the opaque filament. However, in contrast to the conclusions drawn by Gopalswamy, Hanaoka and Lemen (1998) as well as by Hanaoka and Shinkawa (1999), subsequent increase of the mean brightness temperature at 17 GHz may not be evidence for a heating of the filament. This follows from the previous paragraph: the quiet Sun and radio sources show up through gaps in the body of the expanding filament whose optical thickness decreases progressively. Observations at 5.7 GHz do not provide decisive evidence for the possible heating of cold material of filaments. Nevertheless, these observations reveal the presence of a hot plasma above the eruptive filament rather than inside it (Section 2.1.1).

2.1.1. *Brightening wave ahead of the eruptive filament*
Measurements of the average brightness temperatures at 5.7 GHz over small areas of the solar disk covered with the eruptive filament reveal a brightening wave. The brightening wave is not detectable in Fig. 2 because the effect on the solar disk does not exceed the level of fluctuations, but it is well visible in time profiles of average brightness temperatures over nine square areas $1' \times 1'$ (Fig. 5). Their centers are equidistantly arranged along the $S - S$ line in Fig. 3. Curves in Fig. 5 are labeled according to the positions of these regions in Fig. 3 from left to right. To suppress the fluctuations, which are the largest for areas close to the limb due to jitter of images (because of instrumental problems), the time profiles are smoothed over five points. In particular, the passage of the eruptive filament across a weak radio source on the west limb (N30 W90) starts with an increase of its brightness temperature (Fig. 5, upper plot), and only after that does it drop down to the brightness temperature of cold material of the eruptive filament. A most prominent brightening occurs in the limb source where it is not visible in a two-dimensional image.

Lines 1–3 correspond to areas on the quiet Sun. Line 4 corresponds to the region of transition from the quiet Sun to the radio source on the west limb. Line 5 describes the limb area containing the northern part of the limb source. Line 6 shows the area of transition from the solar limb to regions outside of the limb (lines 7–9).

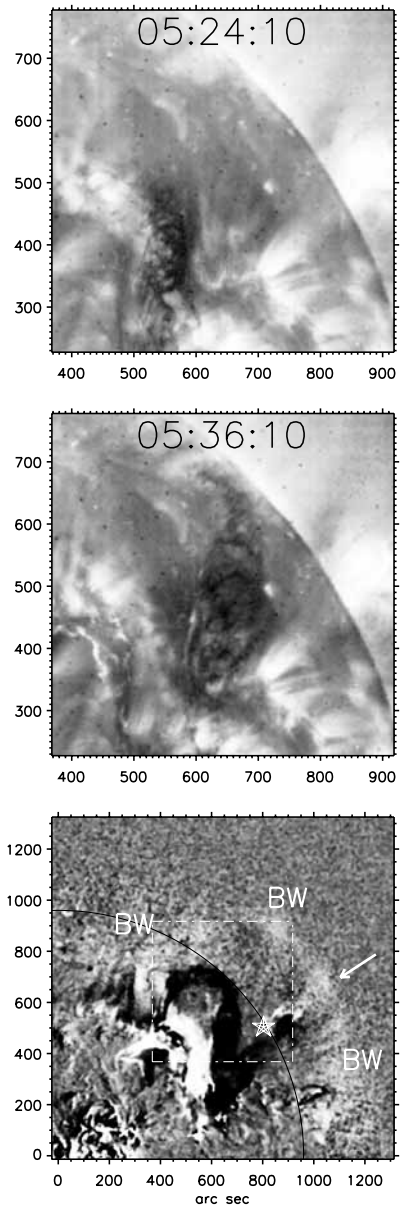

Figure 4. SOHO/EIT 195 Å images of the eruptive filament. The region shown in two upper panels is marked by a white frame in the lower panel. *Top*: The rising filament starts to detach itself from the solar surface. The filament has a sharp leading edge, but has not yet a sharp rear edge. *Middle*: The filament has already detached itself from the solar surface, and its rear edge has become sharp. *Bottom*: Difference image produced by the subtraction of two upper images. Brightening wave (BW) is well visible ahead of the eruptive filament. The microwave limb source is shown by a star.

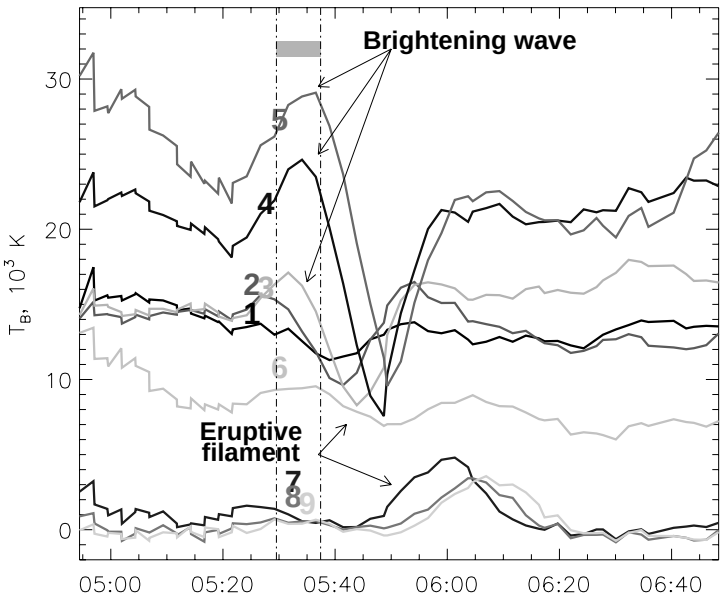

Figure 5. Time profiles of average microwave brightness temperatures over nine square areas $1' \times 1'$ equidistantly arranged along the S–S line in Fig. 3. The horizontal bar marks an expected position of the microwave brightening wave crossing the limb source and corresponds to the light bar $t_2^\star - t_1^\star$ in Fig.6.

The curves clearly show that the brightening wave is not an effect of either the imaging or calibration technique. Furthermore, the brightening wave cannot be associated with any sidelobe of a source inasmuch as (a) the area around the west-limb radio source is located beyond the sidelobes of any bright source, (b) the sidelobes of the filament itself are lower because of its large size, and the sidelobe value is $\leq$22%, which cannot account for the observed brightening. So the brightening wave cannot be due to any instrumental effect.

The brightening wave is detectable also in areas of the quiet Sun (lines 2 and 3). It certainly exists and runs ahead of the eruptive filament. The motion of the brightening wave is seen from the shift of the corresponding maximums indicated by the arrows in Fig. 5, curves 2–5. The slower motion of the eruptive filament is well visible from the shift of the corresponding minimums in the same curves. The brightening wave suggests the presence of a plasma front ahead of the traveling cold eruptive filament, hot and dense enough, but optically thin. Its thermal microwave emission contributes to the effect observed at 5.7 GHz. This contribution is probably insufficient to account for the brightening of the compact limb source (upper curve 5). This appreciable additional brightening is likely due to refraction effects of its

emission in the moving plasma front ahead of the filament. However, large-scale sources well wider than the SSRT beam are not affected by the refraction effects. The quiet Sun is among them. In principle, a microwave burst could occur in the limb source at this time. However, we see that the brightening wave definitely moves, which cannot be associated with a brightening in a compact local source.

The presence of the brightening wave is confirmed by SOHO/EIT 195 Å images. Fig. 4 (bottom) shows a difference image produced by the subtraction of two upper images. The brightening wave (BW) is well visible ahead of the eruptive filament. An essential inhomogeneity of the brightening is detectable in extreme ultraviolet (EUV) along the wave front which expands nearly radially. One of the brightening regions is indicated by the arrow in Fig. 4. One can see that this region crosses the S–S line in Fig. 3 near the microwave limb source shown in Fig. 4 by a star. The high amplitude of the brightening wave in the curve 5 (Fig. 5) is likely determined by both the own emission of the local inhomogeneity in the wave (observed in EUV) and refraction effects.

The identity of the brightening wave visible in microwave and EUV with the formed frontal structure of the CME is confirmed by a time-height plot shown in Fig. 6. The lines 1 (thick dashed) and 2 (solid) show 1^{st} and 2^{nd} degree fit of LASCO data extrapolated down to the distances from the solar disk center of $r = R/R_\odot < 2$. We used for the calculation the LASCO height-time digital data according to the SOHO LASCO CME CATALOG. The data for the fastest segment of the leading edge of the CME on 4 September 2000 were obtained within the position angles of $PA = 315^\circ - 324^\circ$ and within the distances of $r = (3.3 - 28) \times R/R_\odot$. The triangles are the first two points of the LASCO height-time digital data. The linear-fit speed of the CME's frontal structure is $V_1 \approx 850$ km s^{-1} (line 1). The 2^{nd} degree fit (line 2) gives the acceleration of 7.27 m s^{-2} with the speed of $V_2 \approx 758$ km s^{-1} at $r = 1$. The square shows the position of the brightening wave observed in EUV at 05:36:10 UT. The maximum of its brightness is observed at the distance of $r \approx 1.26 - 1.3$ within the position angles $PA \simeq 300^\circ - 320^\circ$ (see Fig. 4, bottom). The light horizontal bar $t_2^\star - t_1^\star$, which connects the intersection points of the lines of the 1^{st} and 2^{nd} degree fit with the line $r = 1$, shows an expected position of the microwave brightening wave crossing the limb source (curve 5 in Fig. 5). This bar is also shown in Fig. 5. One can see that both the microwave and EUV brightening waves are within the interval between the 1^{st} and 2^{nd} degree fits of the LASCO height-time plots. Note that the microwave limb source has $PA = 302^\circ$, whereas the LASCO plots were obtained for $PA \geq 315^\circ$. However, this difference of the position

angles is not important because of large angular width of the CME ($\approx 145°$).

The dark horizontal bar $t_2^0 - t_1^0$ is between the intersection points of the lines of the 1^{st} and 2^{nd} degree fit with the line $r = 0.7$ (this bar is also shown in Fig. 8.). This distance corresponds to the initial position of the filament (the first image in Fig. 3) within $PA \simeq 300° - 315°$. A slow motion of the filament started about half an hour before $t_2^0 =$ 05:26 UT. After about 05:30 UT, a rapid eruption of the filament started. Before this, from about 04:55 UT by about t_2^0, the magnetosphere above the filament expanded with a speed significantly less than V_1, V_2. Its slow motion across the limb source is a possible reason for the large width of the microwave brightening wave in Fig. 5.

We also computed both the 1^{st} and 2^{nd} degree fits of the distance-time plots including EIT data. This results in a slight decrease of the intervals $t_2^0 - t_1^0$ and $t_2^\star - t_1^\star$. In summary, despite of possible errors of measurements and assumptions, there is a fairly good correspondence of the microwave and EUV brightening waves, and the white-light CME frontal structure as well. A possible role of the brightening wave in the dual-filament initiation of CMEs is considered in *Discussion*.

2.2. CME-associated flare

The two-ribbon flare evolved at the initial location of the eruptive filament (see Figs. 2 and 3). In microwaves, it started at about 05:30 UT near the bend of the initial filament. Only two compact radio sources, the eastern **A** and western **B** (shown in Figs. 2 and 3), correspond to the flare for some time. After 05:40 UT, the flare ribbons expanded out of these sources. The ribbons visible at 5.7 GHz correspond quite well to those in the Hα image of 06:32 UT (Fig. 1). The development of the flare and formation of post-flare loops after the filament eruption are also clearly traceable in a SOHO/EIT 195 Å movie.

The approximate coincidence of the effective beam size for NoRH and SSRT during the observations allows us to estimate directly the ratio of brightness temperatures $T_b = T_{b(\text{Observed})} - T_{b(\text{Quiet Sun})}$ for the sources **A** and **B** at 5.7 and 17 GHz. The time profiles of the brightness temperatures of radio bursts at these two frequencies are similar, and their ratio is $\alpha \equiv T_b(5.7)/T_b(17) \approx 8.1 - 9.5$. The proximity of α to $(5.7/17)^{-2} \approx 9$ indicates a thermal character of optically thin radio sources. This is also confirmed by an independent estimation of the optically thin microwave bremsstrahlung computed from soft X-ray GOES data. The electron temperature and emission measure were calculated following a standard technique (Sylwester et al., 1995). The estimate of the thermal free-free emission reproduces quite well both

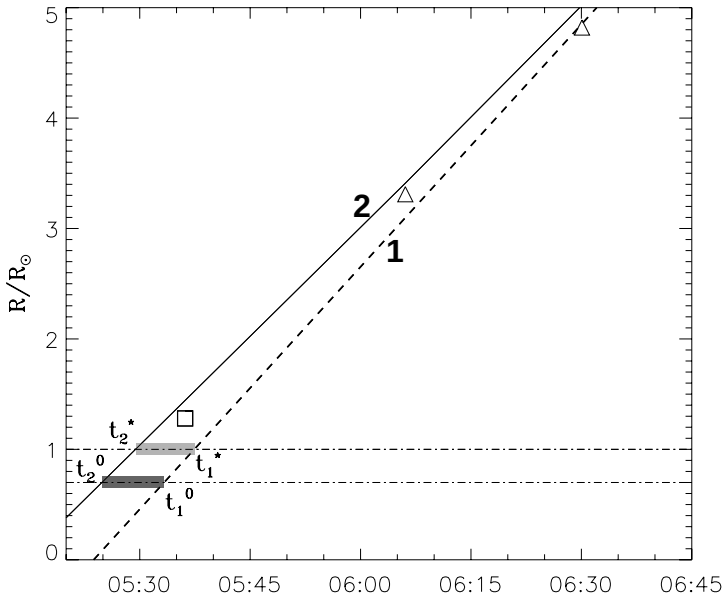

Figure 6. Extrapolations of the 1^{st} (thick dashed) and 2^{nd} (solid) order LASCO height-time plots down to the distances from the solar disk center of $r = R/R_{\odot} < 2$. The triangles are the first two points of the LASCO height-time digital data. The square shows the position of the brightening wave observed in EUV (see Fig. 4). The light horizontal bar $t_2^{\star} - t_1^{\star}$ shows here and in Fig. 5 an expected position of the microwave brightening wave crossing the limb source (curve 5 in Fig. 5). The dark horizontal bar $t_2^0 - t_1^0$ marks the interval between the intersection points of the 1^{st} and 2^{nd} degree fits with the line $r = 0.7$ (also shown in Fig. 8.)

the time profile and the total flux values of the flare emission observed at 5.7 GHz.

It is possible to ascertain the sign of circular polarization for the eastern 5.7 GHz source **A** near the peak of the radio burst. This source was right-handedly polarized, and the degree of polarization of $\simeq 5\%$ exceeds the errors of measurements. Comparisons of NoRH and SSRT images with Kitt Peak magnetograms (03 Sept. at 15:55 UT and 04 Sept. at 16:37 UT) as well as magnetograms obtained with SOHO/MDI (04 Sept. at 04:48 UT and 06:24 UT) reveal that the sources **A** and **B** are localized on different sides of the photospheric inversion line. In accordance with the observed sign and degree of circular polarization, the eastern thermal source **A** is projected onto the N-polarity region with a maximal longitudinal magnetic field $B_{||} \approx 140$ G (06:24 UT), and the brightest western source **B** is projected onto the S-polarity region with $B_{||} \approx -90$ G. The degree of circular polarization of this source is low, within errors of measurements. Nevertheless, at the maximum of the radio burst, the source **B** is dominated by the left-

handed polarization corresponding to the major S-polarity. An analysis of SOHO/EIT 195 Å movie reveals a correspondence of the sources **A** and **B** to bright knots in the EUV flare images. These knots like the microwave sources **A** and **B** appeared at the onset of the flare, and they were connected with a short bright loop. This fact provides also indirect evidence for the opposite signs of circular polarization of the sources **A** and **B**.

The correspondence of the signs of circular polarization in these sources to the major polarity of the magnetic field on both sides of the inversion line implies the following important conclusion. The flare was triggered not by the detachment of filament barbs, as could be expected if the sources **A** and **B** had reverse signs of circular polarization. This conclusion is based on the fact that the footpoints of the filament barbs correspond to regions of minor polarity of the magnetic field (Martin, 1998a). The legs of a filament, in turn, usually correspond to the major polarity of the magnetic field on both sides of the photospheric inversion line. The positions and signs of polarization of the microwave sources **A** and **B** suggest their possible association with the legs (N1 and S2 in Fig. 9 correspond to them) of two different filaments which, nevertheless, were observed as a single filament (lower left corner in Fig. 9). However, in this case *a second eruptive filament must exist.*

2.3. Dual-filament structure of the eruptive prominence

Actually two fragments of the initial eruptive filament are present, and they form a dual-filament structure. In Fig. 7 (right) this dual-filament structure is clearly seen in microwaves above the solar limb (SSRT, 05:57 UT; see also the last images in Figs. 2 and 3). The bulk of the eruptive prominence is concentrated in the western filament (**W**), which is better seen in microwaves both on the solar disk and above the limb. This fragment of the eruptive prominence is also better visible in SOHO/EIT 195 Å images. The movement of the fainter eastern filament (**E**) outside the solar limb is traceable in microwaves when viewing a 5.7 GHz movie, but it is difficult to trace the **E** and **W** fragments separately on the solar disk where their envelope is seen as the initial eruptive filament in first five panels of Figs. 2 and 3.

The eruptive prominence appears as an expanding dual-filament structure in LASCO/C2 images as well. This structure consists of two contacting eruptive filaments sequentially disposed along the edge of the occulting disk (Fig. 7, left; 06:54 UT). The filaments are distinctly connected to each other. The frontal structure (white arrow) of the CME is also visible. We emphasize that the frontal structure of the

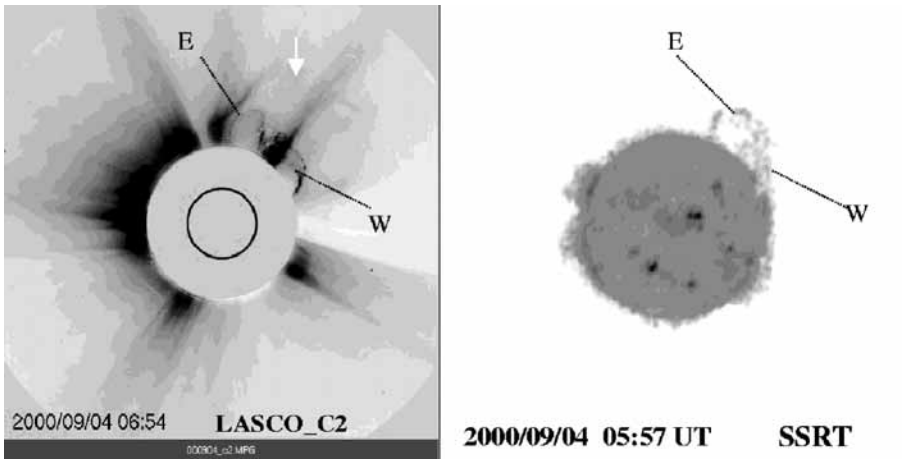

Figure 7. Left: LASCO/C2 image, 06:54 UT, 04/09/2000. The eruptive prominence is seen on north-west as an expanding dual-filament structure. The frontal structure of the CME (white arrow) is also visible. The black circle inside the occulting disk corresponds to the solar limb. *Right*: 5.7 GHz image of this dual-filament structure just above the solar limb. SSRT, 05:57 UT, 04/09/2000. The lines indicate the eastern (**E**) and western (**W**) eruptive filaments. The bulk of the eruptive prominence is concentrated in the western filament.

CME at its early appearance in LASCO/C2 images (e.g., at 06:06 UT) resembles the dual-filament shape of the eruptive prominence.

2.4. "Barbs" in the eruptive filament's structure

Prior to the eruption, the filament does not reveal any helical structure in 5.7 GHz and EUV. During the filament eruption, the formed helix-like shape is visible in EIT images (Fig. 4). The shape of the filament becomes similar to a rope with sharp edges which are also well visible at 5.7 GHz (Fig. 3, 05:47 UT, when the filament is on the solar disk. This part of the filament is actually invisible in EUV at 05:48 UT.) The absence of any pronounced helical structure of the filament prior to the eruption and its formation during the eruption is known from Hα and EUV observations (e.g., Kučera and Antiochos, 1999). It is clear that magnetic reconnection modifies the magnetic topology during the eruption in some way. The question is: *how does a helical structure originate—due to magnetic reconnection of the filament barbs or due to reconnection of coronal loops?* (e.g., Martin, 1998b; Kučera and Antiochos, 1999). SSRT observations can help to answer this question. Before the acceleration phase, the eruptive filament is attached to the solar surface with several black strips. They are detectable in Fig. 3 at 05:19 and 05:27 UT. Obviously they are filament barbs visible in microwaves. Their direction is the same as the direction of the filament

barbs observed in Hα, which are detectable in Fig. 1 (top) on the left side of the filament. The 5.7 GHz image of the filament at 05:27 UT resembles also the sketch of a right-bearing (dextral) filament in the northern hemisphere in *Fig. 10b* from the paper by Martin (1998a). During the eruption observed at 5.7 GHz throughout the entire set of images, this filament barb structure is distinctly transformed into the main body of the eruptive filament. This transformation is accompanied by the appearance of the rear edge of the eruptive filament, and the helical structure can also be detected in 5.7 GHz movies. So the SSRT observations support the supposition that the internal structure of the eruptive filament originates due to the reconnection of the filament barbs. If so, then the appearance of the rear edge of the filament (after about 05:30 UT at 5.7 GHz) means that this reconnection is completed, and the filament barbs are detached from the solar surface. The detachment of the filament barbs completes the formation of the eruptive filament itself, and it determines the helicity sign of its magnetic fields (right-helical twist in our case).

2.5. Apparent velocity of the eruptive filament

Curves R0, R1, R2 and R3 in Fig. 8 show the time profiles of the radial distances between some elements of the eruptive filament and the center of the solar disk. The initial positions of these elements are labeled 0–3 in Fig. 3. The radial component of the projected velocity of the filament can be estimated from the slopes of the curves. The horizontal dashed line shows the solar limb. The horizontal bar in Fig. 8 corresponds to the dark bar $t_2^0 - t_1^0$ in Fig.6. The transition occurs in this interval from the slow motion of the filament to its rapid eruption. The radial component of the projected velocity of the filament increases as high as 250 km s^{-1}, at least for the curves R0, R1 and R2, and remains nearly constant thereafter. The vertical solid line marks the time by which the detachment of the filament barbs from the solar surface is completed (see the previous Section). This time is within the interval $t_2^0 - t_1^0$ as expected.

3. Summary and Discussion

The above analysis suggests the following summary on the event under discussion. A cursory consideration of the observational data can produce the impression that the scheme where the eruptive filament is represented by a single expanding loop-like filament (see, e.g., *Fig. 3* in the review by Forbes (2000) is consistent with the event. However,

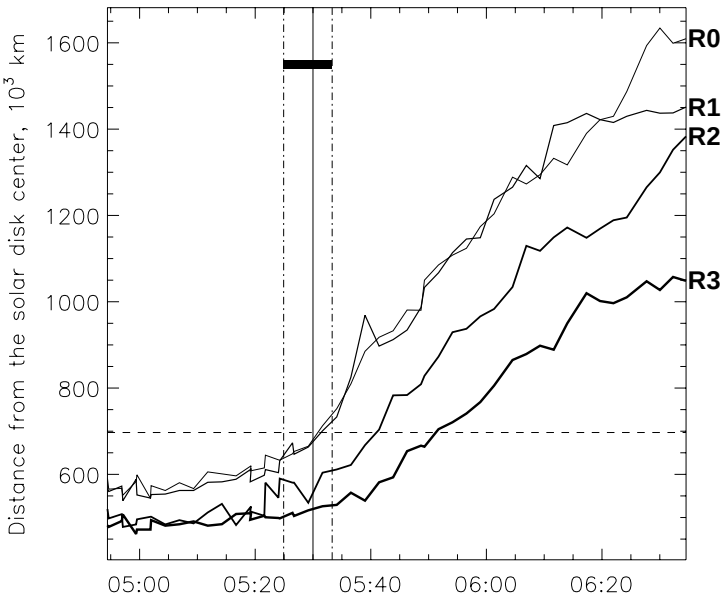

Figure 8. Curves R0, R1, R2 and R3 (thin to thick) show time profiles of the radial distance for some elements of the eruptive filament. Their initial positions are labeled 0–3 in Fig. 3. The horizontal dashed line shows the solar limb. The horizonal bar corresponds to the dark bar $t_2^0 - t_1^0$ in Fig. 6. The vertical solid line marks the time by which the detachment of the filament barbs from the solar surface is completed.

there are actually two filaments, and they form an expanding dual-filament structure (Section 2.3). This does not contradict both the position and polarization of the microwave sources **A** and **B** preceding the development of the "classical" flare ribbons. The observed signs of circular polarization for these sources rule out also the possibility that they originate in a reconnection of filament barbs (Section 2.2). On the other hand, the detachment of the filament barbs is responsible for the formation of the helical structure of the eruptive filament (Section 2.4). This correlates with the acceleration of the eruptive filament (Section 2.5). And, finally, the brightening wave runs ahead of the eruptive filament and kinematically correlates with the frontal structure of the CME (Section 2.1.1).

Below we briefly present our model for the initiation of the observed coronal mass ejection and CME-associated flare. Next, we explain in Section 3.1 some elements of this model including driving forces.

The situation before the eruption is shown schematically in the lower left corner of Fig. 9. The initial quiescent filament consisted of two segments, usual dextral filaments in the northern hemisphere (or two filaments in the southern hemisphere). The cross-interaction of legs of

the filaments goes on. The eruptive phenomenon is interpreted as a situation which occurs after a long contact of these dextral filaments. Only two barbs of the right-bearing filament are shown. Pairs of filament barbs lying on both sides of the photospheric inversion line are magnetically connected with each other. Overlying coronal loops are left-skewed. There exists a flux of long magnetic field lines B_ℓ connecting two segments. We shall call henceforth the magnetic field B_ℓ as the *backbone field*. The backbone field flux Φ is located between the barbs+filament system from below and coronal loops from above. It is shown schematically in both panels of Fig. 9. There is also a longitudinal electric current J_ℓ along the backbone magnetic field. The direction of this current corresponds to the observed inclination of the barbs to the axis of the filament, and to the inclination of the coronal loops above this axis. The helicity of the backbone electric current is $h = 4\pi(\mathbf{B}_\ell\mathbf{J}_\ell)/\mathbf{c} < \mathbf{0}$ for dextral filaments (for sinistral filaments, it is positive, $h > 0$).

The two dextral filaments tend to merge together to form a single long filament. This results in a slow upward motion of the dual-filament system. The attachment of the filament to the photosphere by barbs and by overlying coronal arcades prevents this magnetic system from upward expansion. The initial upward motion is caused by the backbone magnetic field of the merging filaments (*first driving factor*). The flux Φ of this field slowly increases due to magnetic reconnection of the cross-interacting legs of the filaments (N1 and S2 in Fig. 9 correspond to them). If a total length of the resulting dual-filament system is large enough, then the filament barbs start to detach themselves from the solar surface, possibly due to magnetic reconnection between the barbs with oppositely directed magnetic fields. The reconnection of the filament barbs completes the formation of the eruptive filaments themselves, and it determines the helicity sign of their magnetic fields (not shown in Fig. 9). The appearance of the magnetic helical structure creates an additional upward-directed force (*second driving factor*). Acting together, the first and second driving factors lead to the acceleration of the dual-filament system. If the lifting force of these driving factors is sufficient to extend substantially the overlying coronal magnetic arcades, then magnetic reconnection starts below the eruptive filaments (the site labeled X in Fig. 9) in accordance with the classical scheme, and the *third driving factor* comes into play. Herewith the two-ribbon flare starts. Any inefficient operation of each previous driving factor rules out a next one. If this is the case, then the eruptive filament cannot ascend above some height that is sometimes observed.

There are other experimental evidence and phenomenological scenarios which provide a general support for the proposed scheme of

initiation of CME and CME-associated flares. A rapid change in the magnetic connectivity of two different segments of an Hα filament system and formation of a long filament before its eruption was observed by Kim et al. (2001; see the scenario in *Figure 4* from this paper). A very similar scenario for the initiation of eruptive flares is developed by Moore (2001). They propose a Tether-Cutting model and demonstrate its efficiency to interpret Yohkoh/SXT data. The main point of this model is the complete magnetic reconnection of crossed sheared loops, and the filament, if exists, is somehow suspended above the reconnection site. The Tether-Cutting model can be considered as a simplified version of the scenario proposed in our paper. Note that our model considers the filament eruption beyond any active region.

3.1. Driving forces for CME

There are obvious factors which prevent upward expansion of the filament, i.e. (a) the overlying coronal arcades (see, e.g., Antiochos, DeVore and Klimchuk, 1999), and (b) the attachment of the filament to the photosphere via numerous filament barbs whose total magnetic flux is, probably, comparable with the flux of the longitudinal magnetic field inside the filament. As follows from Sections 2.4 and 2.5, factor (b) is important. The presence of the backbone magnetic field is one of the factors which potentially balance the effect of the factors (a) and (b). We classify the role of gravity, including the possible appearance of buoyancy forces, as well as static and dynamic plasma pressures as secondary factors. So we do not discuss them here.

The increase of the backbone magnetic field flux Φ is due to the production of long field lines B_ℓ in the course of reconnection of the cross-interacting legs of two filaments (or, more precisely, the magnetic envelopes of these legs). In this case, the appearance of new field lines proceeds in the same manner as in flare models with the cross-interaction of current-carrying magnetic loops (see, e.g., Sakai, 1996 and references therein; Uralov, 1990a, 1990b; Melrose, 1997). In particular, the formation of a long magnetic filament from a set of loops which undergo forced reconnection was discussed by Uralov 1990a. We are interested not just in the reconnection process, but mainly in the participation of the environment in this process. The longer the merging filaments are, the stronger is the influence of the environment. This fact has not attracted proper attention in previous studies.

The lifting force (*first driving force*) of the slowly increasing flux Φ of the backbone field has the same origin as the force which appears due to shear motion of the footpoints of a magnetic arcade. Let us show this. Each loop-like magnetic flux tube within the arcade with

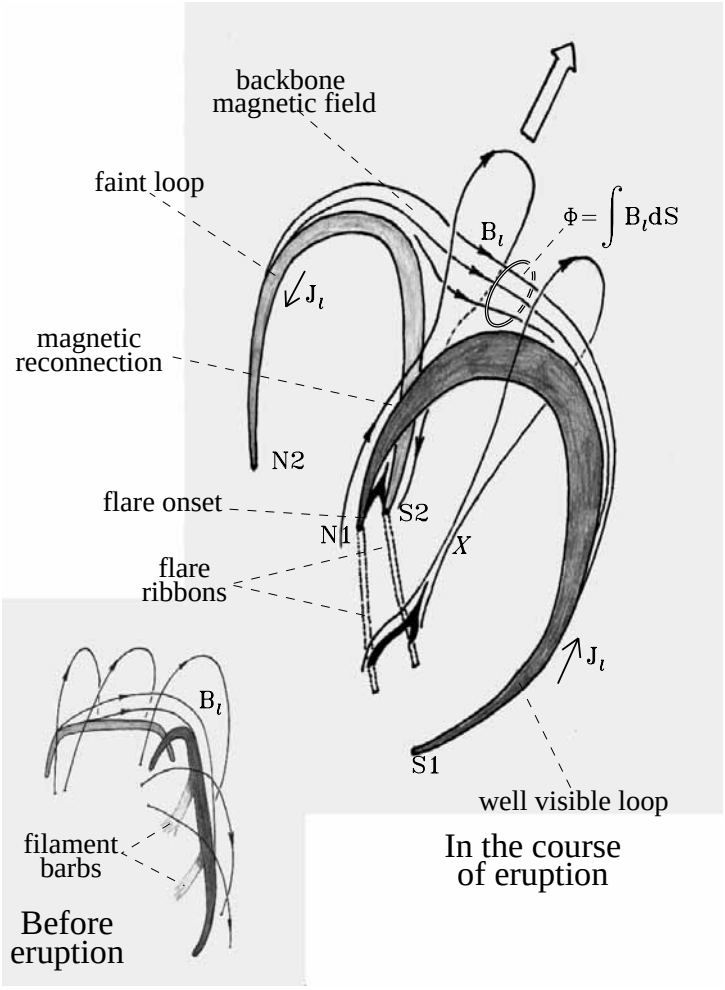

Figure 9. The situation before the eruption is shown in the lower left corner. The initial filament consists of two segments, ordinary dextral filaments. Only two filament barbs are shown. The "backbone" magnetic field B_ℓ connects these filaments. The upward expansion of this magnetic system is prevented by the attachment of the filament to the photosphere by barbs and overlying coronal arcades. The initial upward motion is caused by the backbone magnetic field of merging filaments (*first driving factor*). The flux Φ of this field increases slowly due to magnetic reconnection ("canceling") of the cross-interacting filaments' legs. The filament barbs start to detach themselves from the solar surface due to magnetic reconnection between the barbs with oppositely directed magnetic fields. The detachment of the filament barbs completes the formation of the eruptive filament itself, and it determines the helicity sign of its magnetic fields (not shown). This creates an additional upward-directed force (*second driving factor*). If the lifting force of the first and second driving factors is sufficient to extend substantially the overlying coronal arcades, then magnetic reconnection (label X) starts below the eruptive filament in accordance with the classical scheme, and the *third driving factor* comes into play.

a flux ψ can be characterized by a dipole magnetic moment $\mathbf{m} = \psi\mathbf{d}$, where the vector-distance $\mathbf{d}$ is directed from the S-polarity footpoint to the N-polarity footpoint of the loop. With small shear, the value of $\mathbf{d}$ increases simultaneously for all loops constituting the arcade. A total magnetic moment somewhat increases. A slight increase of the height of all loops within the arcade corresponds to a new equilibrium state.

When reconnection of two cross-interacting identical loop-like magnetic flux tubes occurs, a total magnetic moment $m = 2\psi d$ of the system is conserved, but it undergoes a substantial redistribution. Two new loop-like flux tubes appear instead of the two old ones (see, e.g., Sakai, 1996 and references therein; Uralov, 1990a, 1990b; Melrose, 1997). They are: a short loop with a footpoint separation of b, and a long loop with the footpoint separation of $(2d - b)$. The height of the new short loop-like magnetic flux tube is reduced in accordance with the acquired value of $m = \psi b$. The magnetic moment $\psi(2d - b)$ of the long flux tube, in turn, is increased by a factor of almost 2 if $b \ll d$. Unlike the small lengthening of all field lines in the previous case of shear motions of the arcade footpoints, in this case there is a substantial lengthening of a small number of field lines of the reconnected magnetic flux. The number of such lines increases, and they form the growing flux of the backbone magnetic field. The new equilibrium state of the system depends also on the magnitude of the electric current within the loops before and during the reconnection. We neglected this latter factor in our discussion.

The cross-interaction of the filaments still does not imply eruption, even in the case of their complete reconnection. If the factors (a) and (b), which prevent expansion of the magnetic system, are conserved, then the newly formed long filament will only rise up to a certain height. This is the only outcome in such a case. But what do we actually infer from the observations? The stage of the slow rise involves detachment of the filament barbs from the solar surface. So the retarding factor (b) disappears. After that, the filament's body takes a shape of an isolated, curved magnetic rope. However, the story is not yet completed. The appearance of a helical magnetic structure creates additional force directed upward (*second driving force*). We cannot calculate the actual magnitude of this force, but it is easy to understand its origin by taking well-known equilibrium conditions of a thin toroidal magnetic rope. In the simplest case of a shielded rope outside of which there are no electric currents, the force directed along the major radius of curvature per unit volume is (Solov'ev and Uralov, 1979): $F_R = (\kappa - 2)\overline{B_\ell^2}/8\pi R$, where $\kappa = \overline{B_\varphi^2}/\overline{B_\ell^2}$ is the twist index of the magnetic rope, R is the major radius of curvature, and $\overline{B_\ell^2}$ & $\overline{B_\varphi^2}$ are the squares of the longitudinal

B_ℓ and azimuthal B_φ components of the magnetic field averaged over a cross-section of the rope. Within the approximation which we use, F_R does not depend on the magnitude of the magnetic field and plasma pressure outside of the magnetic rope. The last two parameters are involved in the equilibrium condition along the minor radius of the rope which merely implies a total pressure balance on the surface of the rope. It is also remarkable that the force F_R is determined by the mean value $\overline{B_\varphi^2}$, irrespective of the distribution of longitudinal electric currents within the rope and irrespective of the helicity sign of the magnetic field. It is the increase of $\overline{B_\varphi^2}$ caused by the detachment of the filament barbs which is responsible for the appearance of an additional force F_R directed upward. As a result, the filament barbs are transformed from a preventor into supporter of the expansion process.

The same metamorphosis is also in store for the overlying coronal loops whose magnetic reconnection starts below eruptive filaments in accordance with the classical scheme (see, e.g., *Fig. 3* in Forbes (2000), and Fig. 9). The reconnection between sheared coronal loops leads to formation of a coronal helical magnetic structure (e.g., Gosling, 1990) surrounding the eruptive filaments (which have, in turn, their own helical structure). The appearance of this new helical structure creates also a force directed upward. This force is an addition to the force F_R considered just above. Furthermore, the number of reconnected coronal loops is progressively increased and stimulates a further upward expansion of the eruptive filament. On the other hand, the number of overlying coronal field lines, which prevent the expansion process, decreases by the same value. When combined, these factors may be regarded as a *third driving factor*.

In the dual-filament initiation model under discussion, the filament eruption and the solar flare occur within a simple bipolar magnetic configuration. The initial magnetic field surrounding the filament can be more complex, e.g., have a quadrupolar configuration. The question arises: *Is the large-scale quadrupole magnetic configuration (QMC) favorable for a successful development of a CME and solar flare?* Using QMC, Antiochos, DeVore and Klimchuk (1999) suggest a breakout model (BM) for a CME initiation assuming two crucial factors. One of them implies large shear motions of photospheric footpoints of low current-carrying arcade. The other factor appears because the ascending arcade is located under an X-separator of a QMC. The combined action of these two factors gives rise to a thin horizontal current sheet instead of the X-separator, and magnetic reconnection within this sheet determines the subsequent evolution of the entire magnetic system. On the other hand, Uralov et al. (2000) employed a model very similar to BM in their analysis of the evolution of the quadrupole magneto-

sphere of an active region prior to LDEs. In spite of the attractiveness and simplicity of the breakout model, the presence of a distinct shear motion in the event of 4 September 2000 is doubtful. The shape and length of the observed filament persisted unchanged during at least 8 days before the eruption. Nevertheless, combining our dual-filament initiation model with the breakout model seems fruitful. To combine them, it is sufficient to place the scheme of Fig. 9 at the base of a large-scale QMC.

We propose the idea of the possible role of the frontal structure of a CME in our model. In Section 2.1.1. we have established a kinematic correspondence of the brightening wave observed in microwaves and EUV with the CME frontal structure. Here we assume an association of the brightening wave with the backbone magnetic field. If so, then the CME frontal structure originates not far from the eruptive filament. The presence of coronal dimming in the difference of the soft X-ray images at 06:06:16 UT and 04:34:08 UT somewhat away from the pre-eruptive position of the filament (H. Hudson, private communication) supports this statement. As we have pointed out, the current helicity of the backbone magnetic field is negative ($h < 0$) for a dextral filament. Such field lines have left-helical twist. By virtue of chirality rules (Martin, 1998a), the same sign of the twist also corresponds to the helical magnetic field produced due to magnetic reconnection in ascending coronal arcades. These two large-scale structures are likely to determine the sign of total helicity of the CME. On the other hand, the helicity of the eruptive filament, which is inside of those large-scale structures, is determined by chirality rules for filament barbs rather than for coronal arcades (Section 2.4). The eruptive filament's helicity has the opposite sign with respect to the total CME's helicity.

Summarizing this Section, we conclude that the cause of a solar flare and coronal mass ejection can be the interaction of filaments or magnetic ropes. In particular, some initial upward motion is caused due to merging of two short filaments into a long one. If the new filament is long enough, its subsequent motion has the character of a magnetohydrodynamic instability. The instability consists of three stages, to which the *first*, *second* and *third driving factors* correspond. Magnetic reconnection is important during each of these stages. As a consequence, magnetic structures, which have initially kept the filament near the solar surface, now become supporters of its ejection into interplanetary space. As we have observed, the CME-associated flare started well after the eruption. In some sense, the flare was triggered by the filament ejection. Actually all of them are episodes of a single process.

Acknowledgements

The data used here became available to us thanks to efforts of colleagues operating Nobeyama Radioheliograph, Big Bear Solar Observatory, Kanzelhoehe Solar Observatory, the MDI, EIT & LASCO instruments onboard SOHO mission, cooperative efforts of NSF/NOAO, NASA/GSFC, and NOAA/SEL. The CME catalog which we referred to is generated and maintained by the Center for Solar Physics and Space Weather, the Catholic University of America in cooperation with the Naval Research Laboratory and NASA. SOHO is a project of international cooperation between ESA and NASA.

We are indebted to Dr. H. Hudson for his analysis of the Yohkoh/SXT data related to the event under discussion. We thank V.G. Mikhalkovsky for his assistance in preparing the English version of the manuscript. We are grateful to an unknown referee for important comments which aided in improvement of this paper.

This research was partly supported by the Russian Foundation for Basic Research (grants 00-02-16456, 00-15-96710, 01-02-16290), the Russian Ministry of Science & Technical Policy (No. 0-27), and the Federal Scientific Program "Astronomy".

References

Antiochos, S. K., DeVore, C. R. and Klimchuk, J. A.: 1999, *Astrophys. J.*, **510**, 485.

Forbes, T.G.: 2000, *J. Geophys. Res.*, **105 (A10)**, 23153.

Gary, D. E.: The microwave structure of quiescent solar filaments at high resolution, California Institute of Technology (private communication).

Gopalswamy, N.: 1999, *Solar Physics with Radio Observations*, Proceedings of the Nobeyama Symposium 1998, Edited by T. Bastian, N. Gopalswamy and K. Shibasaki, NRO Report **No. 479**, 141.

Gopalswamy, N., Yashiro, S. and Plunkett, S.: 1999, *Solar Physics with Radio Observations*, Proceedings of the Nobeyama Symposium 1998, Edited by T. Bastian, N. Gopalswamy and K. Shibasaki, NRO Report **No. 479**, 207.

Gopalswamy, N., Hanaoka, Y. and Lemen, J.R.: 1998, *New Perspectives on Solar Prominences, IAU Colloquium 167, ASP Conference Series*, **150**, 358.

Gosling, J.T.: 1990, *Physics of Magnetic Flux Ropes*, AGU Geophysical Monograph, **58**, 343.

Hudson, H.: 1999, *Solar Physics with Radio Observations*, Proceedings of the Nobeyama Symposium 1998, Edited by T. Bastian, N. Gopalswamy and K. Shibasaki, NRO Report **No. 479**, 159.

Hanaoka, Y., Kurokawa, H., Enome, S., Nakajima, H., Shibasaki, K., Nishio, M. et al.: 1994, *Publ. Astron. Soc. Japan.*, **46**, 205.

Hanaoka, Y. and Shinkawa, T.: 1999, *Astrophys. J.*, **510**, 466.

Kim, J.-H., Yun, H.S., Lee, S., Chae, J., Goode, P.R. and Wang, H.: 2001, *Astrophys. J. Let.*, **547**, L85

Krissinel, B.B., Kuznetsova, S.M., Maksimov, V.P., Prosovetsky, D.V., Grechnev, V.V., Stepanov, A.P., Shishko, L.F.: 2000, *Publ. Astron. Soc. Japan.*, **52**, 909.

Kučera, T.A. and Antiochos, S.K.: 1999, Proceedings of 8th SOHO Workshop *Plasma dynamics and diagnostics in the solar transitional region and corona, ESA SP-446*, October 1999, 97.

Maia, D., Vourlidas, A., Pick, M., Howard, R., Schwenn, R., Magalhães, A.: 1999, *J. Geophys. Res.*, **104**, 12507.

Martin, S.F.: 1998a, *Solar Physics*, **182**, 107.

Martin, S.F.: 1998b, *New Perspectives on Solar Prominences, IAU Colloquium 167, ASP Conference Series*, **150**, 419.

Maksimov, V.P. and Nefedyev, V.P.: 1992, *Ann. Geophysicae*, **10**, 354.

Melrose, D.B.: 1997, *Astrophys. J.*, **486**, 521.

Moore, R.L., Sterling, A.C., Hudson, H.S. and Lemen, J.R.: 2001, *Astrophys. J.*, **552**, 833

Pick, M.: 1999, *Solar Physics with Radio Observations*, Proceedings of the Nobeyama Symposium 1998, Edited by T. Bastian, N. Gopalswamy and K. Shibasaki, NRO Report **No. 479**, 187.

Pohjolainen, S., Maia, D., Pick, M., Vilmer, N., Khan, J.I., Otruba, W., Warmuth, A., Benz, A., Alissandrakis, C., Thompson, B.J.: 2001, *Astrophys. J.*, **556**, 421.

Sakai, J.I. and de Jager, C.: 1996, *Space Sci. Rev.*, **77**, 1.

Sylwester, J., Garcia, H.A. and Sylwester, B.: 1995, *Astron. Astrophys.*, **293**, 577.

Švestka, Z.: 1999, Proceedings of 8th SOHO Workshop *Plasma dynamics and diagnostics in the solar transitional region and corona, ESA SP-446*, 61.

Solov'ev, A.A. and Uralov, A.M.: 1979, *Soviet Astronomy Letters*, **5**, 250.

Uralov, A.M.: 1990a, *Solar Physics*, **127**, 253.

Uralov, A.M.: 1990b, *Physics of Magnetic Flux Ropes*, AGU Geophysical Monograph, **58**, 285.

Uralov, A.M., Nakajima, H., Zandanov, V.G. and Grechnev, V.V.: 2000, *Solar Physics*, **197**, 275.

Zandanov, V.G. and Lesovoi, S.V.: 1999, *Solar Physics with Radio Observations*, Proceedings of the Nobeyama Symposium 1998, Edited by T. Bastian, N. Gopalswamy and K. Shibasaki, NRO Report **No. 479**, 37.

Zandanov, V.G., Lesovoi, S.V. and Uralov, A.M.: 1999, *Structure and Dynamics of the Solar Corona*, Proc. Intern. Conf. on Solar Physics (in memory of Professor G.M. Nikolsky), Troitsk, Moscow Region, October 1999, 236 in Russian.